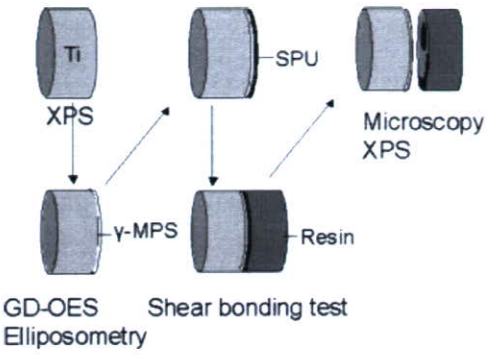

Figure 2. Flow chart of the experimental procedure.

X-ray photoelectron spectroscopy

Composition and thickness of the surface oxide film on the Ti disk was determined using XPS (SSX100, SSI, UK). Also, the fractured manner and chemical bonding state at the fractured surface after the shear bonding test of Ti-SPU composites with and without the γ-MPS layer were characterized. The conditions for the XPS analysis are listed in Table II. The take-off angle for photoelectron detection from the surface of the specimen was 35°. All binding energies, given in this paper are relative to the Fermi level, and all spectra were excited with the monochromatized Al Kα line (1486.61 eV). The spectrometer was calibrated against Au $4f_{7/2}$ (binding energy, 84.07 eV) and Au $4f_{5/2}$ (87.74 eV) of pure gold and Cu $2p_{3/2}$ (932.53 eV), Cu $2p_{1/2}$ (952.35 eV), and the Cu Auger $L_3M_{4,5}M_{4,5}$ line (kinetic energy, 918.65 eV) of pure copper. The energy values were based on published data.[26] The composition and thickness of the surface layer and the composition of the metal substrate were simultaneously calculated according to a method devised by Asami et al.[27,28] Empirical data and theoretically calculated data of relative photoionization cross-sections were used for the quantification. The relative photoionization cross-sections used in this study are summarized in Table III, where σ_{ij}/σ_{O1s} represents the relative photoionization cross-section of a level j electron of an element i to that of the O 1s electron.[27,28] Data obtained from XPS experiment was statistically analyzed by Student's t test.

TABLE I
The γ-MPS Concentration and Immersion Time of Specimens Used for GD-OES, Ellipsometry, Shear Bonding Test, and XPS

Immersion Time (min)	Concentration of γ-MPS Solution (vol %)			
	0.1	0.5	1.0	2.0
0 (untreated)	E, S, X			
1	G, E, S, X	E, S	G, E, S	E, S
10	E	E	E, S	E, S
50	E	E	E, S	E, S
100	E	E	G, E, S	E

G, GD-OES; E, Ellipsometer; S, Shear Bonding Test; X, XPS.

TABLE II
Conditions for XPS Analysis

X-ray source	Al Kα
Accelerating voltage (kV)	10
Current (mA)	30
Take-off angle (°)	35
Measurement area (μm)	1000 × 1000
Vacuum (Torr)	$>1.7 \times 10^{-9}$

Glow discharge optical emission spectroscopy

The depth profiles of elements from the γ-MPS layer were determined using a GD-OES instrument (Jovin Yvon RF 5000GD-OES, HORIBA, Japan) with a power of 40 W in a 600 Pa argon atmosphere. The spectral wavelengths (nm) employed for detecting various elements were as follows: H, 121.57; C, 156.14; N, 149.26; S, 185.25; Si, 288.15; Ti, 365.35; and O, 130.00.[29,30] The sputtering rate was constant to directly compare these depth profiles obtained from different surfaces.

Ellipsometry

The thickness of the γ-MPS layer was determined with an ellipsometer (DVA-36Ls, Mizojiri Optical, Japan) in air. A He-Ne laser was used as the light source with a wavelength of 632.8 nm, and the incident angle to the Ti surface was 70°. The thickness was calculated by the optical constants of the refractive index and the absorption coefficient of titanium oxide on the Ti substrate, 2.209 and 3.079, respectively.

Shear bonding test

The shear bonding strength of the Ti/γ-MPS/SPU interface of the Ti-SPU composite was evaluated using a universal mechanical test machine (2000-IB, Shimadzu, Japan) with a crosshead speed of 0.1 mm min^{-1} at ambient. The apparatus for the test was originally designed as shown in Figure 3. The shear bonding stress, σ, was calculated by the following equation:

$$\sigma = P / A$$

where P is the shear bonding force and A is the original bonding area. After the shear bonding test, the fractured surface was observed using an optical microscope. The area of SPU occupying the fractured surface was measured using a personal computer with an imaging analysis program (NIH Image 1.62 program), and the SPU area fraction on the gross fractured surface area was cal-

TABLE III
Photoionization Cross-Sections of Level j of Element i Relative to that of O 1s, σ_{ij}/σ_{O1s}

Level	σ_{ij}/σ_{O1s}
Photoionization cross-section	
Ti $2p_{3/2}$	1.28
C 1s	0.34

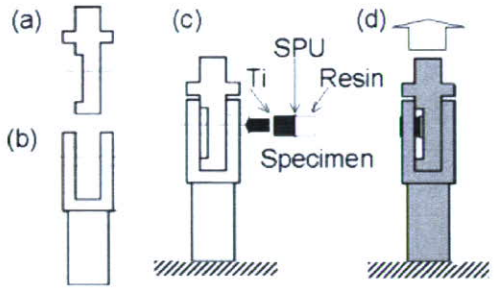

Figure 3. Illustration of the apparatus for the shear bonding test: (a) sliding and (b) fixed part. The Ti-SPU composite is inserted through both holes in parts (a) and (b), which are arranged in a straight line (c). By pulling up the sliding part, shear stress was applied onto the bonding interface of the composite (d).

culated. Data obtained from shear bonding test was statistically analyzed by one-way ANOVA.

RESULTS AND DISCUSSION

Composition and thickness of surface oxide film on Ti

From the C 1s spectra, it was concluded that none of the specimens contained carbonate because no peak was detected at an energy region of 289–290 eV where carbonate should give a C 1s peak.[31] Therefore, carbon detected by XPS can be ascribed to so-called contaminant carbon. Apart from carbon, only titanium and oxygen were detected with XPS. The Ti 2p electron energy region peak gave four doublets according to valence, Ti^0, Ti^{2+}, Ti^{3+}, and Ti^{4+} according to published binding energy data [Fig. 4(a)].[32] Proportions of Ti^0, Ti^{2+}, Ti^{3+}, and Ti^{4+} were 0.01, 0.02, 0.03, and 92.8, respectively. On the other hand, the O 1s electron energy region peak contained three peaks originating from O^{2-}, hydroxide or hydroxyl groups, OH^-, and hydrate and/or adsorbed water, H_2O [Fig. 4 (b)].[33] Proportions of O^{2-}, OH^-, and H_2O in the surface oxide film were 0.54, 0.29, and 0.18, respectively. The relative concentrations of titanium and oxygen were calculated assuming the gross

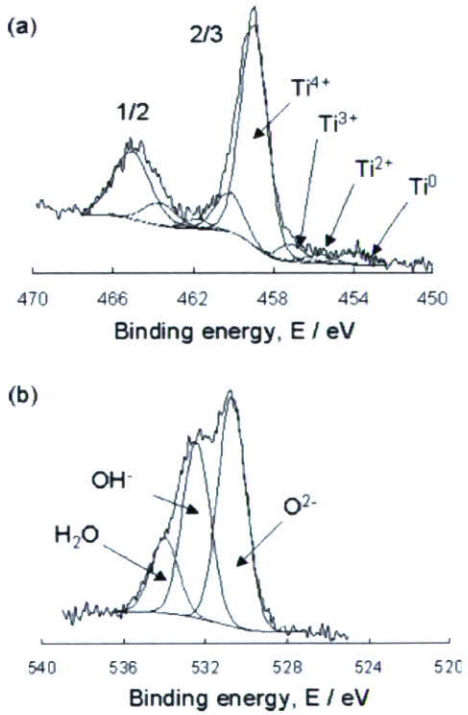

Figure 4. Typical XPS spectra of Ti 2p and O 1s electron energy region and the deconvolution of these peaks: (a) Ti 2p and (b) O 1s.

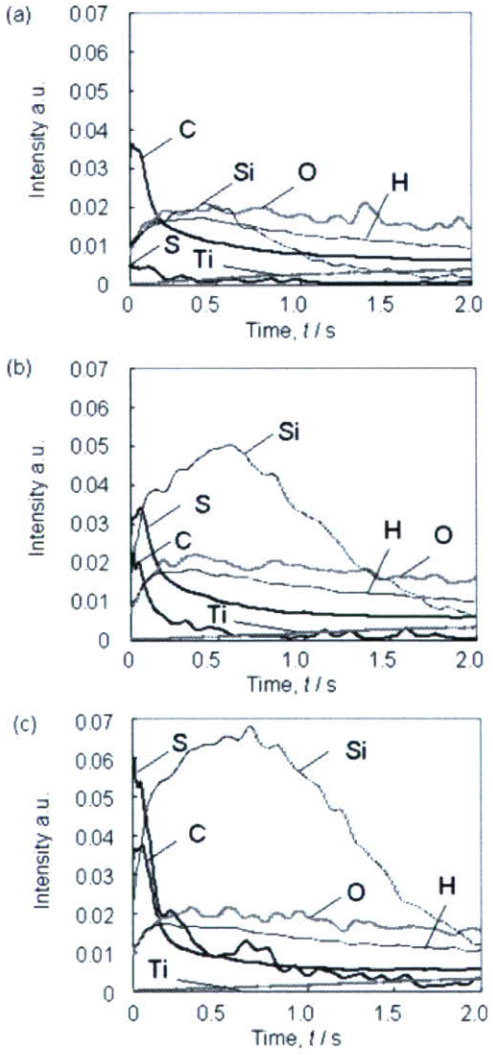

Figure 5. Depth profiles of elements in the γ-MPS layer formed by immersion in a 0.1% γ-MPS solution for 1 min (a), a 1.0% γ-MPS solution for 1 min (b), and a 1.0% γ-MPS solution for 100 min (c), as determined by the GD-OES.

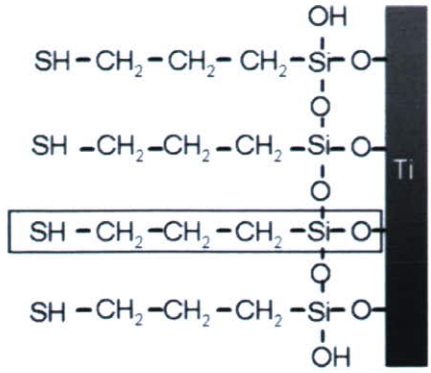

Figure 6. Chemical structure of the γ-MPS layer bonded to a Ti surface. The black frame indicates one molecular unit of γ-MPS.

amount of these elements as detected using XPS was 100 mole percent; 25.2 and 74.8mol%, respectively. The thickness of the surface oxide film was calculated as 4.8 nm. Therefore, chemical composition was calculated as $TiO_{0.59}(OH)_{0.85}{\cdot}0.53H_2O$. These results indicate that the Ti disk is covered by a very thin titanium oxide mainly consisting of TiO_2 with a small amount of Ti^{2+} and Ti^{3+}. A large amount of hydroxyl groups exist on and inside the surface oxide.

Depth profile and thickness of the γ-MPS layer

The depth profiles of elements in the γ-MPS layer determined by the GD-OES are shown in Figure 5. Similar depth profiles were obtained from all specimens. Elements were detected from the outside to the inside in this order: sulfur, carbon, silicon, and titanium. Sulfur and carbon were considered to the mercapto group of the γ-MPS. In addition, silicon in the hydrolysis γ-MPS chemically combined with hydroxyl groups on the Ti disk and Si—O—Ti bonding was formed. These results are in good agreement with the chemical structure of γ-MPS bonded to a Ti surface (Fig. 6) that is expected from the general structure of γ-MPS. The intensity of sulfur in the γ-MPS layer increased with the increase of the concentrations of the γ-MPS solution and immersion times (Fig. 7). In other words, one sulfur atom exists on the terminal of a molecular unit of γ-MPS (as shown in Fig. 6); therefore, the number of sulfur directly correlate with the numbers of the molecular unit. In other words, the number of the γ-MPS molecular unit increases with the increase of the concentration of γ-MPS and the immersion time.

The thickness of the γ-MPS layer varied with the concentration of the γ-MPS solution and the immersion time (Fig. 8). In spite of the increase in the immersion time, the thickness of the γ-MPS layer did not significantly increase when the Ti disk was immersed in 0.1, 0.5, and 1.0% γ-MPS solutions. However, the thickness increased dramatically with the immersion time when the Ti disk was immersed in a 2.0% γ-MPS solution. The thickness of the γ-MPS layer decreased at 100 min of immersion time. In other words, the γ-MPS layer does not always thicken, even when the immersion time is increased.

Since many molecular units exist in a γ-MPS solution with high concentration, immobilization by dehydration and condensation of the molecular unit to the Ti surface easily occurs. Furthermore, possibility of immobilization of the γ-MPS molecular unit to the Ti surface increases with the immersion time. As a result, the thickness of the γ-MPS layer increased with the concentration of the γ-MPS solution and the immersion time.

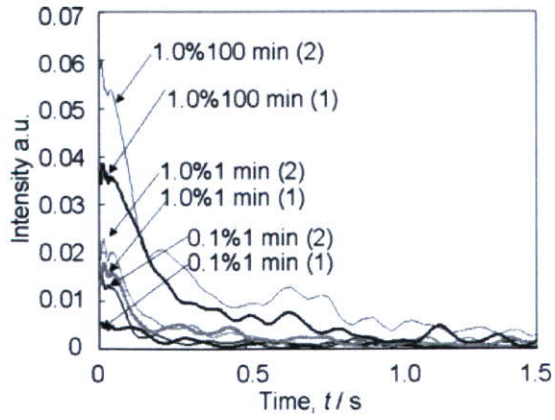

Figure 7. Depth profiles of sulfur of the γ-MPS layer as the concentration of γ-MPS solution and immersion time. Numbers, (1) and (2), in the figure represent two different specimens prepared under the same condition.

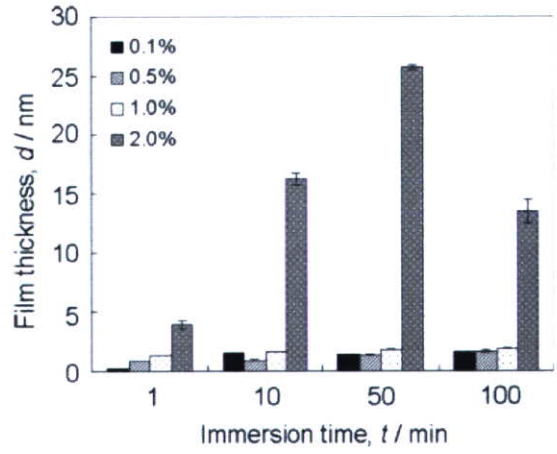

Figure 8. Thickness of the γ-MPS layer as the concentration of γ-MPS solution and immersion time.

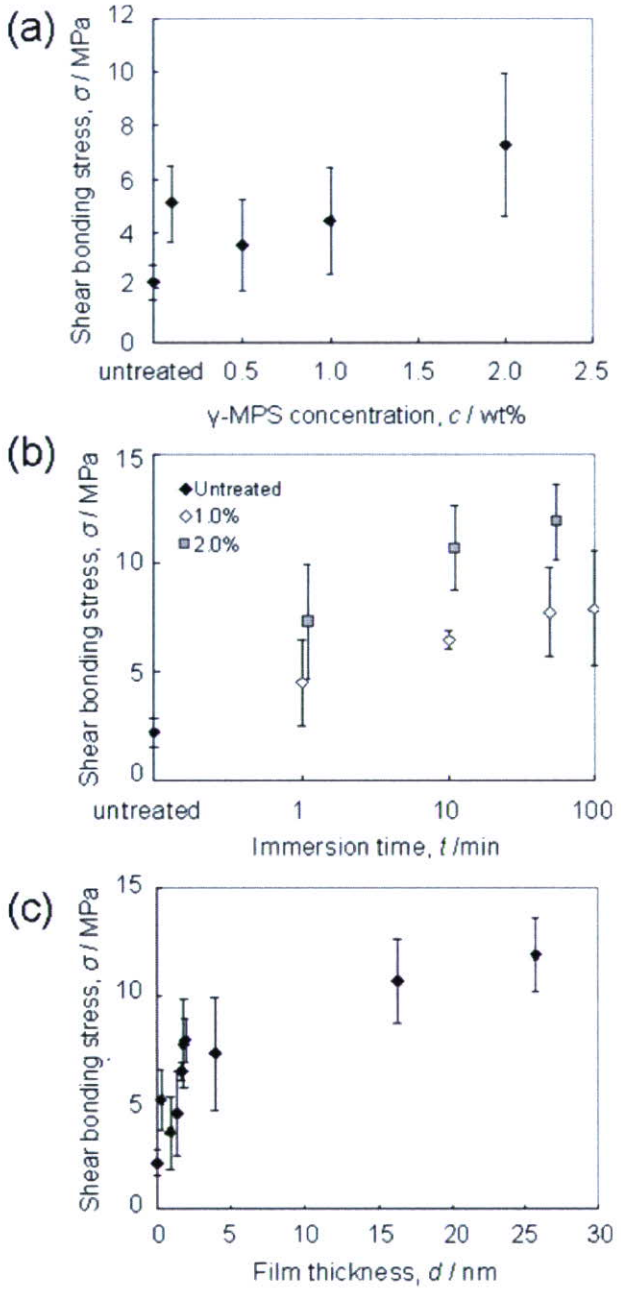

Figure 9. Shear bonding stress of the Ti/γ-MPS/SPU interface formed by immersion for 1 min in various concentrations of a γ-MPS solution (a) and immersion in a 1.0 and a 2.0% γ-MPS solution at various immersion times (b). Relationship between the shear bonding stress of the Ti/γ-MPS/SPU interface and the thickness of the γ-MPS layer (c).

Shear bonding stress of the Ti/γ-MPS/SPU interface

Shear bonding stress of Ti/γ-MPS/SPU interface increased with the increase of the concentration of the γ-MPS solution only in the case of 1-min immersion [Fig. 9(a)], while no significant difference was obtained. On the other hand, the shear bonding stress of the Ti/γ-MPS/SPU interface formed from 1.0 and 2.0% γ-MPS solutions significantly increased with immersion times ($p < 0.05$) as shown in Figure 9(b). Kanie et al. claimed that the adhesive strength of the PMMA resin against the Co—Cr alloy using γ-MPS increased with an increase in the concentration of γ-MPS,[20] which supports the results reported above. In addition, the relationship between the shear bonding stress of the Ti/γ-MPS/SPU interface and thickness of the γ-MPS layer is shown in Figure 9(c). The shear bonding stress significantly increased with the thickness of the γ-MPS layer ($p < 0.05$).

The chemical structure of the Ti/γ-MPS/SPU interface is illustrated in Figure 10. The length of one molecular unit is more than 1 nm according to the distances between atoms. If the number of molecular units per Ti surface area is small, each molecular unit keeps a distance from its neighbors and consequently falls down to the Ti surface. This results in a thin γ-MPS layer. Also, —Si—O—Si— bonding network among molecular units is not sufficiently formed. On the other hand, if the number of molecular units per Ti surface area is large, the molecular units will crowd at the interface and stand perpendicular to the Ti surface. As a result, the thickness of the γ-MPS layer will increase. In this case, the —Si—O—Si— bonding network is sufficiently formed. A thick γ-MPS layer would be attributable to the increase in the shear bonding strength because a thick γ-MPS has more molecular units containing S—H groups bonded to SPU.

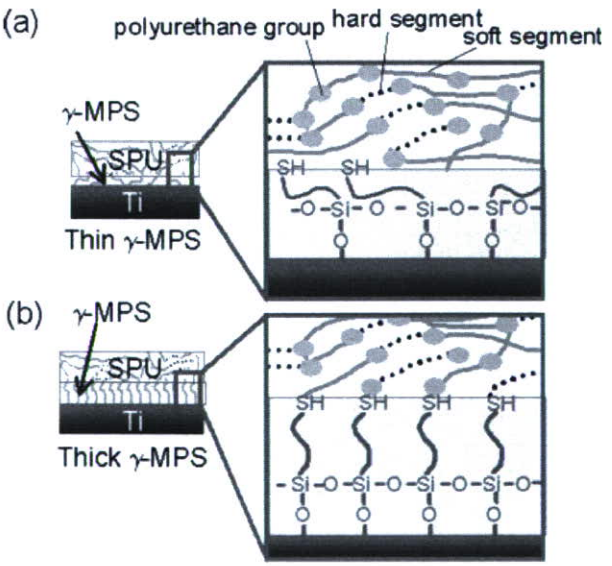

Figure 10. Schematic chemical structure at the Ti/γ-MPS/SPU interface in the case of a thin γ-MPS layer (a) and a thick MPS layer (b).

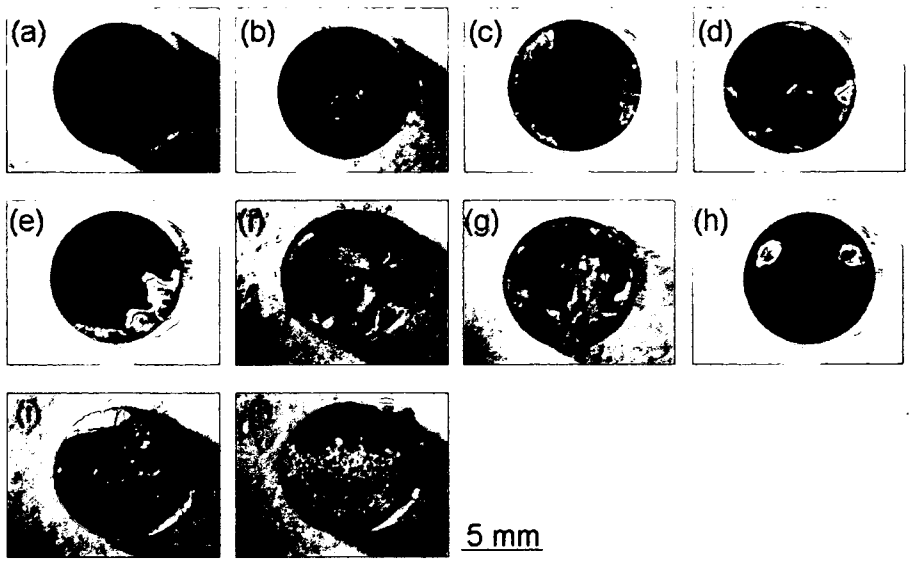

Figure 11. Optical microscopic images of the fractured surface of the Ti-SPU composite. Untreated (a), immersion in 0.1, 0.5, 1.0, and 2.0% γ-MPS for 1 min (b, c, d, and h), in 1.0% γ-MPS for 10, 50, and 100 min (e, f, and g), and 2.0% γ-MPS for 10 and 50 min (i and j).

Fractured surface observation

Optical microscopic images of the fractured surface of the Ti-SPU composite are shown in Figure 11. The SPU area fraction depended on the concentration of γ-MPS and the immersion times. Figure 12(a,b) show the SPU area fraction to the total fractured surface area. The SPU area fraction increased with the increase of the concentration of the γ-MPS solution and immersion time, while no significant difference was observed. Figure 12(c) shows the shear bonding stress of the Ti-SPU composite interface in relation to the SPU area fraction to the total fractured surface area of the Ti-SPU composite (R_2 = 0.8051). These results clarify that the shear bonding stress is large when the Ti-SPU composite is fractured inside the SPU. Hibino et al. demonstrated that the shear bonding stress at the interface between a dental alloy and a resin increases when the composite of a dental alloy and resin was fractured inside regin[34] and the result supports this study.

Analysis of the fractured surface by XPS

Carbon, nitrogen, sulfur, silicon, and titanium were detected from the fractured surface using XPS. Typical XPS spectra of C 1s electron energy regions and the deconvolutions of these peaks according to published data[32] are shown in Figure 13. Table IV lists the ratios [C—O, C—N, C=N]/[C], [C=O, OH^-, Si—O—Si]/[O], and [Ti^0]/[Ti] in the C 1s, O 1s, and Ti 2p peaks, respectively, obtained from specimens with and without a γ-MPS layer. The [C—O, C—N, C=N]/[C] ratio was significantly larger in the Ti-SPU composite in the presence of the γ-MPS layer than that in its absence. The C—O, C—N, and C=N peaks were originated from the SPU component elements, not from the γ-MPS layer. In other words, the Ti-SPU composite was fractured leaving the SPU component elements on the fractured surface. However, more residual SPU on the fractured surface of the Ti-SPU composite with the γ-MPS layer existed than that without a γ-MPS layer. Regardless of the existence of the γ-MPS layer, the Ti^0 state was detected from the fractured surface. The Ti^0 peak originated from the Ti substrate. Therefore, the SPU layer remaining on the fractured surface was very thin (less than 10 nm). In addition, the [C=O, OH^-, Si—O—Si]/[O] ratio in the O 1s peaks was slightly larger in the Ti-SPU composite with the γ-MPS layer than in that without the γ-MPS layer, but this is not statistically significant. The Si—O—Si peak originated from the γ-MPS layer. In other words, the γ-MPS layer between the Ti substrate and residual SPU remained.

The relative concentrations of carbon, nitrogen, oxygen, sulfur, silicon, and titanium in the specimens were calculated, and it was assumed that the gross volume of these elements detected by XPS was 100mol%. Table V represents the concentrations of carbon, oxygen, and titanium of the fractured surfaces of the Ti-SPU composite with and without the γ-MPS layer. The carbon concentration was significantly higher in the Ti-SPU composite with the γ-MPS layer than in that without it. Moreover, a large

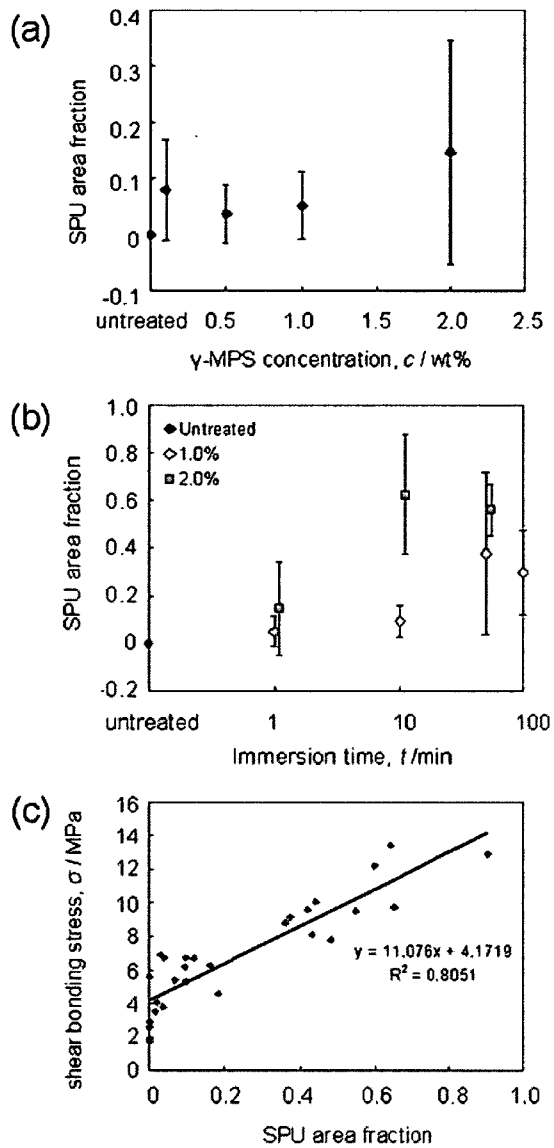

Figure 12. SPU area fraction to the total fractured surface area of the Ti-SPU composite through the γ-MPS layer formed by immersion for 1 min in various concentrations of the γ-MPS solution (a) and immersion in a 0.1 and a 2.0% γ-MPS solution at various immersion times (b). Shear bonding stress of the Ti/γ-MPS/SPU interface in relation to the SPU area fraction to the total fractured area of the Ti-SPU composite (c).

amount of SPU remained on the fractured surface of the Ti-SPU composite with the γ-MPS layer rather than in that without it. On the other hand, the oxygen and titanium concentrations decreased in the presence of the γ-MPS layer. The signals from titanium oxide and titanium substrate were small due to the remaining layer. A schematic model of the fractured regions before and after the shear bonding test is proposed according to the results reported

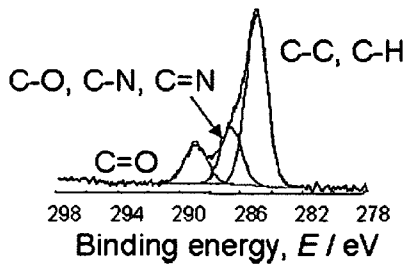

Figure 13. Typical XPS spectra of C 1s electron energy region and the deconvolution of these peaks.

above, as shown in Figure 14. The SPU elements remained on the fractured surface as a result of the presence of the γ-MPS layer. The thicker the γ-MPS layer was, the larger the SPU area fraction on the fractured surface was.

CONCLUSIONS

The thickness of the γ-MPS layer is controlled by the concentration of the γ-MPS solution and the immersion time. The shear bonding stress of the Ti/γ-MPS/SPU interface increased with the increase in the thickness of the γ-MPS layer. The Ti-SPU composite was fractured inside the SPU, and the shear bonding stress of the Ti/γ-MPS/SPU interface increased with the increase in the SPU area fraction. The γ-MPS is very useful to improve the bonding

TABLE IV
Ratios of [C—O, C—N, C=N]/[C], [C=O, Si—O—Si, OH—]/[O], and [Ti^0]/[Ti] in the Fractured Surface of the Ti-SPU Composite

	Area (%)		
	C [C—O, C—N, C=N]	O [C=O, OH^-, Si—O—Si]	Ti [Ti^0]
Without the γ-MPS layer	26.0 (0.2)	44.7 (5.6)	5.2 (0.1)
With the γ-MPS layer	25.5 (0.9)	50.7 (3.8)	6.1 (0.8)

The values given are mean (standard deviation).
*$p < 0.05$ (significant differences between the corresponding values).

TABLE V
XPS Results for the Relative Concentration of Elements in the Fractured Surface of the Ti-SPU Composite

	Concentration (%)		
	C	O	Ti
Without the γ-MPS layer	43.9 (2.0)	42.4 (1.5)	3.9 (0.1)
With the γ-MPS layer	56.9 (1.3)	35.7 (1.2)	2.8 (1.0)

The values given are mean (standard deviation).
*$p < 0.05$ (significant differences between the corresponding values).

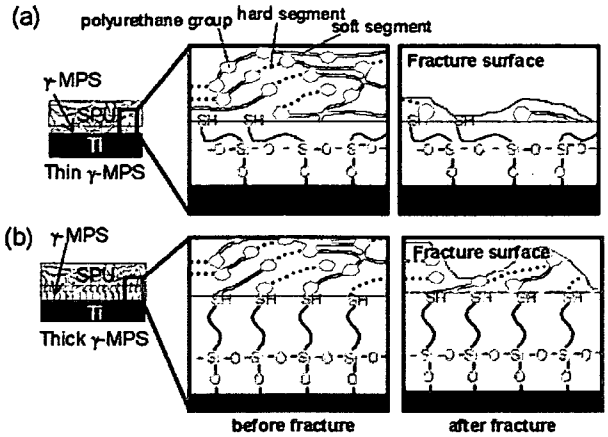

Figure 14. Schematic model of the fractured region before and after the shear bonding test in the case of a thin γ-MPS layer (a) and a thick γ-MPS layer (b).

strength of the Ti-SPU composite. The factor governing the shear bonding strength between Ti and SPU is the thickness of the γ-MPS layer. This study should lead to enhancements in the creation of metal–polymer composites for artificial organs.

We appreciate Ms. Hiroko Kawano, HORIBA, Ltd., for assisting with GD-OES. We are also grateful to Prof. K. Asami, Dr. H. Kimura, and Mr. N. Ohtsu, Institute of Materials Research, Tohoku University, for assisting with XPS. The study was performed under the inter-university cooperative research program of Laboratory for Advanced Materials, Institute of Materials Research, Tohoku University.

References

1. Ratner BD, Hoffman AS, Schoen FJ, Lemons JE. Biomaterials Science: An Introduction to Materials in Medicine. Amsterdam: Elsevier; 2004.
2. Nakabayashi N. Development of Medical Polymers and Materials. Tokyo: CMC Publishing; 1998.
3. Takayanagi H. Technology and Application in Polyurethane. Tokyo: CMC Publishing; 1993.
4. Ishihara K, Hatanaka K, Yamaoka T, Oya Y. Biomaterial Science. Tokyo: Tokyo Kagakudozin; 2003.
5. Khan I, Smith N, Jones E, Finch DS, Cameron RE. Analysis and evaluation of a biomedical polycarbonate urethane tested in an *in vitro* study and an ovine arthroplasty model. II. In vivo investigation. Biomaterials 2005;26:633–643.
6. Khan I, Smith N, Jones E, Finch DS, Cameron RE. Analysis and evaluation of a biomedical polycarbonate urethane tested in an in vitro study and an ovine arthroplasty model. I. Materials selection and evaluation. Biomaterials 2005;26:621–631.
7. Choong SKS, Wood S, Whitfield HN. A model to quantify encrustation on ureteric stents, urethral catheters, and polymers intended for urological use. BJU Int 2000;86:414–421.
8. Kenausis GL, Voros J, Elbert DL, Huang N, Hofer R, Ruiz-Taylor L, Textor M, Hubbell JA, Spencer ND. Poly(L-lysine)-*g*-poly(ethylene glycol) layers on metal oxide surfaces: Attachment mechanism and effects of polymer architecture on resistance to protein adsorption. J Phys Chem B 2000;104:3298–3309.
9. Ishihara K, Ziats NP, Tierney BP, Nakabayashi N, Anderson JM. Protein adsorption from human plasma is reduced on phospholipid polymers. J Biomed Mater Res 1991;25:1397–1407.
10. Miller BH, Nakajima H, Powers JM, Nunn ME. Bond strength between cements and metals used for endodontic posts. Dent Mater 1998;14:312–320.
11. Matsumura H, Nakabayashi N. Adhesive 4-META/MMA-TBB opaque resin with poly(methyl methacrylate)-coated titanium dioxide. J Dent Res 1988;69:1614–1616.
12. Fujishima A, Fujishima Y, Ferracane JL. Shear bond strength of four commercial bonding systems to cpTi. Dent Mater 1995; 11:82–86.
13. Qiu J, Dominici JT, Lifland MI, Okazaki K. Composite titanium dental implant fabricated by electro-discharge compaction. Biomaterials 1997;18:153–160.
14. Rilo B, da Silva JL, Martinez-Insua A, Santana U. A titanium and visible light-polymerized resin obturator. J Prosthet Dent 2002;87:407–409.
15. Taira Y, Imai Y. Primer for bonding resin to metal. Dent Mater 1995;11:2–6.
16. Smith NA, Antoun GG, Ellis AB, Crone WC. Improved adhesion between nickel-titanium shape memory alloy and polymer matrix via silane coupling agents. Compos A 2004;35: 1307–1312.
17. Yoshida K, Matsumura H, Tanaka T, Atsuta M. Properties of titanium dioxide-polymer composite with titanate coupling agents. J Dent Mater 1989;8:629–635.
18. Abboud M, Casaubieilh L, Morval F, Fontanille M, Duguet E. PMMA-based composite materials with reactive ceramic fillers. IV. Radiopacifying particles embedded in PMMA beads for acrylic bone cements. J Biomed Mater Res 2000;53:728–736.
19. Yoshida K, Tanagawa M, Atsuta M. Effects of filler composition and surface treatment on the characteristics of opaque resin composites. J Biomed Mater Res 2001;58:525–530.
20. Kanie T, Arikawa H, Fujii K, Inoue K. Physical and mechanical properties of PMMA resins containing γ-methacryloxyproplytrimethoxysilane. J Oral Rehabil 2004;31:161–171.
21. Ferracane JL, Berge HX, Condon JR. In vitro aging of dental composites in water-effect of degree of conversion, filler volume, and filler matrix coupling. J Biomed Mater Res 1998;42: 465–472.
22. Bexell U, Olsson M, Jhansson M, Samuelsson J, Sundell P-E. A tribological study of a novel pre-treatment with linseed oil bonded to mercaptosilane-treated aluminum. Surf Coat Technol 2003;166:141–152.
23. Bexell U, Olsson M, Sundell P-E, Jhansson M, Carlsson P, Hellsing M. A ToF-SIMS study of linseed oil bonded to mercaptosilane-treated aluminum. Appl Surf Sci 2004231/232: 362–365.
24. Jayaseelan SK, Ooji WJV. Rubber-to-metal bonding by silanes. J Adhes Sci Technol 2001;15:967–991.
25. Zhang F, Kang ET, Neoh KG, Wang P, Tan KL. Surface modification of stainless steel by grafting of poly(ethylene glycol) for reduction in protein adsorption. Biomaterials 2001;22:1541–1548.
26. Asami K. A precisely consistent energy calibration method for X-ray photoelectron spectroscopy. J Electron Spectrosc 1976; 9:469–478.
27. Asami K, Hashimoto K, Shimodaira S. XPS determination of compositions of alloy surfaces and surface oxides on mechanically polished iron-chromium alloys. Corros Sci 1977;17:713–723.
28. Asami K, Hashimoto K. An XPS study of the surfaces on Fe-Cr, Fe-Co, and Fe-Ni alloys after mechanical polishing. Corros Sci 1984;24:83–97.

29. Shimizu K, Habazaki H, Skeldon P, Thompson GE, Wood GC. GD-OES depth profiling analysis of amorphous Ni-P-plated aluminum hard disks. Surf Interface Anal 2000;29:151–154.
30. Fernandez B, Bordel N, Pereiro R, Sanz-Medel A. Radio frequency glow discharge-optical emission spectrometry for direct quantitative analysis of glass. Anal Chem 2004;76:1039–1044.
31. Hammond K, Holubka JW, DeVries JE, Dickie RA. The application of X-ray photo-electron spectroscopy: A study of interfacial composition-induced paint de-adhesion. Corros Sci 1981;21:239–253.
32. Asami K, Chen SC, Habazaki H, Hashimoto K. The surface characterization of titanium and titanium-nickel alloys in sulfuric acid. Corros Sci 1993;35:43–49.
33. Asami K, Hashimoto K. The X-ray photo-electron spectra of several oxides of ion and chromium. Corros Sci 1977;17:559–570.
34. Hibino Y, Kuroiwa A, Kurosawa S, Kanke S, Hashimoto H. Bond strength of dental luting cements to titanium castings. J Dent Mater 1990;9:79–85.

$CaTiO_3$ coating on titanium for biomaterial application—Optimum thickness and tissue response

Naofumi Ohtsu,[1,2] Kenji Sato,[2] Aya Yanagawa,[3] Kesami Saito,[2] Yoshio Imai,[3] Takao Kohgo,[3] Atsuro Yokoyama,[3] Katsuhiko Asami,[2] Takao Hanawa[1]

[1]*Department of Metallurgy, Institute of Biomaterials and Bioengineering, Tokyo Medical and Dental University, Tokyo 101-0062, Japan*

[2]*Advance Research Center of Metallic Glasses, Institute for Material Research, Tohoku University, 2-1-1 Katahira, Aoba-ku, Sendai 980-8577, Japan*

[3]*Department of Oral Functional Science, Graduate School of Dental Medicine, Hokkaido University, Sapporo 060-8586, Japan*

Received 17 January 2006; revised 18 July 2006; accepted 29 September 2006
Published online 5 February 2007 in Wiley InterScience (www.interscience.wiley.com). DOI: 10.1002/jbm.a.31136

Abstract: The objectives of this study were to determine the optimum thickness of a $CaTiO_3$ film for biomaterial applications and to investigate the biocompatibility and bone formation of titanium with a $CaTiO_3$ film. First, $CaTiO_3$ films of 10, 20, 30, and 50 nm in thickness were deposited on titanium substrates using radiofrequency magnetron sputtering followed by annealing at 873 K in air for 7.2 ks. The optimum thickness of the $CaTiO_3$ film for bone formation was determined by comparison with its performance regarding calcium phosphate formation in Hanks' balanced saline solution (HBSS). Regarding calcium phosphate formation, the performance of the specimen with a 50-nm-thick $CaTiO_3$ film was superior to those of specimens with other thicknesses. A titanium prism with a $CaTiO_3$ film of 50-nm in thickness was surgically inserted in both soft and hard rat tissues. The biocompatibility of $CaTiO_3$-deposited titanium and bone formation on it was investigated by histological observations. A slight inflammatory reaction was observed around the titanium with the 50-nm-thick $CaTiO_3$ film, while no severe response, such as degeneration and necrosis, was observed in either soft or hard rat tissue. New bone formation on the titanium plate with the $CaTiO_3$ film was more active than that without the film. The 50-nm-thick $CaTiO_3$ film has biocompatibility and can facilitate new bone formation *in vivo*, and, consequently, it is an excellent surface modification method for biomaterial applications. © 2007 Wiley Periodicals, Inc. J Biomed Mater Res 82A: 304–315, 2007

Key words: biomaterials; titanium; $CaTiO_3$ coating; biocompatibility; bone formation

INTRODUCTION

Titanium and its alloys have been widely used for dental and orthopedic implants because of their excellent biocompatibility[1–4] and good mechanical properties.[5–7] One disadvantage of these materials is that it takes several months to obtain good fixation between the material and bone. Although bulk properties dictate the mechanical properties of biomaterials, tissue-biomaterial processes are surface phenomena, and, as such, they are governed by the surface properties. To shorten the bone-fixation term, therefore, various surface modification techniques have been attempted.

Hydroxyapatite (HAP; $Ca_{10}(PO_4)_6(OH)_2$) is compatible with various tissue types and can bond directly to bone.[8–10] Despite its excellent properties as a biomaterial, HAP lacks mechanical strength for some purposes, especially because of its brittleness and low impact resistance, which sometimes results in failure in implantation.[11] Consequently, major attempts have been conducted to achieve successful physical and chemical coating processes with HAP on titanium to acquire good mechanical properties and excellent bone fixation.[12] Various methods have been used to coat with HAP, such as immersion coating,[13] electrophoretic deposition,[14] ion-beam-assisted deposition,[15] ion-beam sputter coating[16] or radiofrequency (RF) magnetron sputter coating,[17] pulsed laser deposition,[18] and thermal spraying techniques.[19,20] At this point, thermal spraying, especially the plasma-spray method, appears to be the most favorable because it has a high deposition rate and is applicable to complex shapes. In fact, this method is most commonly used in clinical applications. Nevertheless, some disadvantages have resulted in some reluctance to use the plasma-sprayed HAP in clinical settings. The most significant problems are poor coating-substrate

Correspondence to: N. Ohtsu; e-mail: nohtsu@imr.tohoku.ac.jp

bonding[21,22] and lack of uniformity of the coating crystallinity.[23,24] Generally, coatings with low crystallinity degrade rapidly in the human body. Likewise, plasma-sprayed HAP, which has parts with low crystallinity, dissolves rapidly in the human body. Consequently, loss of fixation of the coating-substrate bonding[25] and inflammation of the tissue around the material result. The crystallinity of the coating could increase with postannealing treatment. However, in a calcium-phosphate coating on titanium, the post-annealing treatment causes cracking of the coating,[26,27] and, thus, the post-annealing treatment is not appropriate for the commercially available plasma-sprayed HAP.

One simple method to eliminate these problems would be to use thinner films. The mechanical properties of a film, such as the toughness and coating-substrate-bonding strength, increase with a decrease in the film thickness, and the possibility of film cracking with the post-heat treatment decreases. On the other hand, the thickness of the commercially available plasma-sprayed HAP is about 50 μm in general, which is reported as the optimum thickness.[28,29] Since a dense HAP surface will loosen up to 15 μm because of a dissolution process after implantation, a coating should have a thickness sufficiently exceeding this lower limit and, thus, a thickness of about 50 μm or more is required.[28] Furthermore, the 50-μm-thick HAP would not be susceptible to fatigue failure, which commonly occurs in coatings thicker than 100 μm, but would still result in constant bone growth.[29] Therefore, it is generally considered that the application of HAP films that are much thinner than the commercially available films is inappropriate because the bone-fixation ability of the coatings is rapidly lost.

Recently, some of the present authors reported that calcium-phosphate formation on titanium in Hanks' balanced saline solution (HBSS) was facilitated by coating a $CaTiO_3$ thin film[30]; in this study, the enhancement of calcium-phosphate formation was demonstrated on a $CaTiO_3$ thin film that was deposited to 50-nm thickness using RF magnetron sputtering followed by annealing in air at 873 K. Since biomaterials with the potential for good calcium-phosphate formation can rapidly adhere to bone, the $CaTiO_3$ coating would be expected to impart good bone-fixation qualities to titanium. Because the 50-nm film thickness of the $CaTiO_3$ coating is 1/1000 of the 50-μm thickness, the problems regarding the plasma-sprayed HAP noted above could easily be ameliorated. Moreover, the 50-nm $CaTiO_3$ film was reported to crystallize to a perovskite-type phase.[30] Since the dissolution of a crystallized-$CaTiO_3$ film in a simulated body fluid is rare,[31] ion releases from the $CaTiO_3$ film in the human body would be expected to be rare as well.

In a previous study, the prepared $CaTiO_3$ film thickness was fixed to 50 nm, and all investigations were performed *in vitro*.[30] The effect of the $CaTiO_3$ coating thickness on calcium-phosphate formation has not been investigated yet; in other words, the optimum thickness has not been determined. If it becomes possible to impart good bone fixation to titanium by coating it with a thin $CaTiO_3$ film, the deposition time could most likely be shortened because the deposition time of the film is proportional to the thickness. By thinning the coating film, the mechanical properties of the film would be further improved. Biocompatibility and bone formation *in vivo* have not been evaluated yet. Even if *in vitro* experiments were to suggest that the modification by the $CaTiO_3$ coating is a better alternative to plasma-sprayed HAP, a definitive evaluation would need to be conducted with *in vivo* experiments because a complex physiological reaction cannot be evaluated *in vitro*.

The objectives of this study are to determine the optimum thickness of a $CaTiO_3$ film for calcium-phosphate formation and to investigate the tissue response of $CaTiO_3$-coated titanium, particularly, with regard to bone formation on a titanium plate coated with a $CaTiO_3$ film of the optimum thickness. The optimum thickness of the $CaTiO_3$ film was determined by estimating the calcium-phosphate formation in HBSS. Moreover, the $CaTiO_3$ films were carefully characterized by grazing incident angle X-ray diffractometry (GI-XRD) and Auger electron spectroscopy (AES), and the dissolution behavior in a physiological solution was also investigated by AES. The relationship between the film properties and calcium-phosphate formation was discussed on the basis of the results. After determination of the optimum thickness, the $CaTiO_3$ film with the optimum thickness was surgically inserted in both soft and hard rat tissues. The tissue response and osteogenesis around $CaTiO_3$ were investigated and compared with those around cpTi by histological observation with the use of optical and fluorescent microscopy.

EXPERIMENTAL PROCEDURES

Preparation of specimens for immersion

Commercially available pure Ti (cpTi) grade 2 (ISO 5832-2) with a disk shape (Φ 8 mm × t 1 mm) was mechanically polished with SiC paper (#1500) to obtain a rough surface. $CaTiO_3$ films were deposited on a cpTi substrate using RF magnetron sputtering with a $CaTiO_3$ target in an Ar gas flow. RF magnetron sputtering has several advantages, including homogeneous film preparation and ease of controlling the film thickness. These advantages make it possible to prepare homogeneous high-quality films. On the other hand, the low deposition rate is a disadvantage in RF magnetron sputtering.[16] However, the problem of the low deposition rate is not critically serious because the required thickness of the $CaTiO_3$ film deposited is extremely small.

TABLE I
Specimen Preparation Conditions

Symbols	Deposition Conditions			Postannealing
	Sputtering Power (W)	Deposition Time (ks)	Thickness (nm)	
cpTi	–	–	–	No
anTi	–	–	–	Yes
CT10	200	0.21	10	Yes
CT20	200	0.42	20	Yes
CT30	200	0.62	30	Yes
CT50	200	1.04	50	Yes

The $CaTiO_3$ target used in the sputtering process was prepared by a sintering method. A commercial regent of $CaTiO_3$ with a purification of 99.9% was formed into a 51-mm disk by a cold-press method, and, finally, the $CaTiO_3$ disk was sintered at 1523 K for 10.8 ks. The pressure of the deposition chamber just before the start of sputtering (base pressure) was about 10^{-7} Pa. The sputtering power was fixed at 200 W. The thicknesses of the deposited films were about 10, 20, 30, and 50 nm, which were calculated with the sputtering rate of the $CaTiO_3$ film. Thereafter, the specimens were annealed at 873 K for 7.2 ks in air using an electric furnace. For comparison, cpTi without a coating was examined with and without annealing under the same conditions as for the film-deposited specimens. The conditions for specimen preparation are summarized in Table I.

Characterization of specimens

The prepared specimens before and after the annealing treatment were characterized by the following two methods. The crystallinity of the $CaTiO_3$ film was identified by GI-XRD with a step-scanning mode at 0.8 deg min^{-1} and an X-ray incident angle α = 1.0 degree against the specimen surface (Rotaflex RU-200B, Rigaku, Japan). The in-depth profile of the $CaTiO_3$ film was determined by AES (JAMP-7100E, JEOL, Japan), where the acceleration voltage of the electron probe was fixed to 10 kV and that of Ar ions for ion etching was fixed to 3.0 kV.

The dissolution behavior of the prepared specimens after the annealing treatment was investigated by comparing the in-depth profiles before and after immersion in a 0.8% NaCl solution in which the NaCl concentration corresponds to that of HBSS. Since HBSS contains the Ca ion and, thus, Ca adsorption on the surface of the specimen is often observed after immersion, the NaCl solution was employed to avoid Ca adsorption. The specimens were immersed in the NaCl solution for 14 days. The change in the in-depth profiles by immersion in the solution was determined by AES.

Evaluation of performance regarding calcium-phosphate formation in HBSS

HBSS was employed as a simulated body fluid to evaluate the performance of specimens regarding calcium-phosphate formation because its inorganic content is similar to that of human blood plasma. The HBSS used in this study was prepared without any organic species. The ion concentrations of HBSS are listed in Table II. HBSS was prepared by dissolving a prescribed amount of reagent-grade NaCl, KCl, $CaCl_2$, $MgSO_4 \cdot 7H_2O$, $Na_2HPO_4 \cdot 2H_2O$, KH_2PO_4, and $NaHCO_3$ (Nacalai Tesque) in deionized water (Millipore). No adjustment of the pH was performed. The pH value of the HBSS immediately after preparation was about 7.8. Each of six specimens (Table I) was immersed in 12.6 mL of the HBSS at 310 K. The immersion was performed six times for each preparation condition. While avoiding Si contamination eluted from the vessels,[32] specimens were immersed in vessels made of perfluoroalkoxy fluoroplastic (Teflon©PFA), and the vessels were completely sealed. To avoid an increase in the pH, HBSS was changed once every three days. Three specimens were retrieved from HBSS after immersion for 35 days, and the remaining three specimens were retrieved after immersion for 45 days. After retrieval, these specimens were gently rinsed with distilled water and dried in a convection oven at 313 K.

The performance of each specimen regarding calcium-phosphate formation was estimated by observing the surface and a cross section after immersion using scanning electron microscopy (SEM) and EPMA equipped with wavelength dispersive X-ray spectrometry (WDS) and energy dispersive X-ray spectrometry (EDS). The acceleration voltage of SEM and EPMA was 15 kV. Furthermore, the thickness of the calcium phosphate layer after immersion was estimated with a cross-sectional view when the calcium phosphate layer was sufficiently thick. The thickness was determined by averaging several points of the layer.

Tissue response to rat specimens

Preparation of specimens for implantation

Only on one side of the cpTi with a prism shape (1 mm × 1 mm × 5 mm), $CaTiO_3$ films were prepared with the same method as for CT50. The reason for using 50 nm as the

TABLE II
Ion Concentrations of Hanks Balanced Saline Solution (HBSS)

	Concentration (mol L^{-1})
Na^+	1.42×10^{-1}
K^+	5.81×10^{-3}
Mg^+	8.11×10^{-4}
Ca^{2+}	1.26×10^{-3}
Cl^-	1.45×10^{-1}
HPO_4^{2-}	7.78×10^{-4}
SO_4^{2-}	8.11×10^{-4}
CO_3^{2-}	4.17×10^{-3}

$CaTiO_3$ film thickness is explained later. The surface opposite the deposition side was metallurgically polished with SiC paper (#1500), and the Ti-oxide layer formed by the annealing treatment was then completely removed. This side became equal to the surface of cpTi and used as control against the $CaTiO_3$ film side.

Animal experiment

At first, the specimens were sterilized in an autoclave. Eight male Wistar rats aged 14 weeks (weight about 400 g) were used in this study. After the rats were anesthetized with diethyl ether (Wako Pure Chemical Industries, Osaka, Japan), pentobarbital sodium (50 mg/kg; MEMBUTAL Injection, Dainippon Pharmacy, Osaka, Japan) was injected intraperitoneally. The specimens were inserted into subcutaneous connective tissue in the abdominal region of the rats to examine the response in soft tissue. For hard tissue, a hole with a diameter of about 2 mm was carefully made in the lateral surface of the diaphysis of the femur using a dental round bar with a physiological saline external coolant. The specimen was inserted into the medullary space longitudinally through the hole made in the femur. The specimens were changed in the direction of the surface of cpTi and $CaTiO_3$ and implanted to prevent the influence of the anatomical site and surgical incision. The wound was then sutured, and 2% Calcein (CA; 8 mg/kg, Calcein, Wako Pure Chemical Industries, Osaka, Japan) was injected intraperitoneally. Moreover, 5% oxytetracycline hydrochloride (TC; 20 mg/kg, Terramycin, Pfizer, Tokyo, Japan) was injected into the peritoneal cavity a day before sacrifice. These agents were used for bone labeling.[33] Animal experiments were performed in accordance with the Guide for the Care and Use of Laboratory Animals, Hokkaido University Graduate School of Dental Medicine. No rats were lost in the course of the study.

Histological observation of soft and hard tissue

Rats were sacrificed on days 7 and 28 after implantation, and the specimens with tissue blocks were fixed in 10% neutral-buffered formalin. The specimens implanted in the subcutaneous tissue were carefully removed after fixation, and the tissue blocks were then embedded in paraffin by a conventional method. Hematoxylin- and eosin-stained specimens were observed histopathologically with an optical microscope.

The tissue blocks from the rat femurs were fixed in 10% neutral-buffered formalin, washed, stained with Villanueva bone stain, and then embedded in PMMA. The hard tissue blocks were then sectioned to 400 μm in thickness with a precision saw, and thinner sections of about 100 μm in thickness were prepared by mechanical polishing. The thin specimens were observed with optical and fluorescent microscopy.

RESULTS

Surface characteristics

AES in-depth profiles of specimens with a $CaTiO_3$ film of 50 nm in thickness (CT50) and without a film after the annealing treatment (anTi) are shown in Figure 1. Because of oxidation during annealing, Ti-oxide layers form between the $CaTiO_3$ film and the Ti substrate. The thicknesses of the Ti-oxide layers of CT50 and anTi are about 300 and 600 nm, respectively. Figure 2 shows the in-depth profiles of the Ca-atomic ratio determined by AES in specimens with a $CaTiO_3$ film of 10 (CT10), 20 (CT20), 30 (CT30), and 50 (CT50) nm in thickness before and after annealing, where the Ca-atomic ratio is defined by [Ca]/([Ca] + [Ti]). The profiles show a Ca-rich region at the top of the surface. Film thicknesses of CT10 and CT20 are too small to observe the region in which the Ca-atomic ratio is constant. In the specimens before annealing, the Ca-atomic ratio decreases with an increase in the depth. After annealing, the diffusion of Ca atoms into the direction of the Ti substrate is observed in the profiles of CT10, CT20, and CT30, and the region in which the Ca-atomic ratio was almost constant on CT30 disappears. However, the change in the in-depth profile of CT50 is so small that the Ca-ratio-constant region still remains.

The GI-XRD patterns of the specimens after annealing are shown in Figure 3. Since the effective depth of

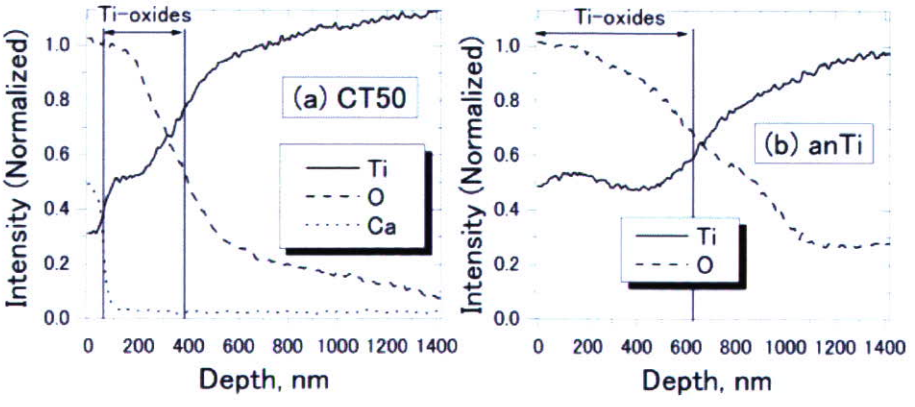

Figure 1. AES in-depth profile of (a) CT50 and (b) anTi. Intensities are normalized to an arbitrary value.

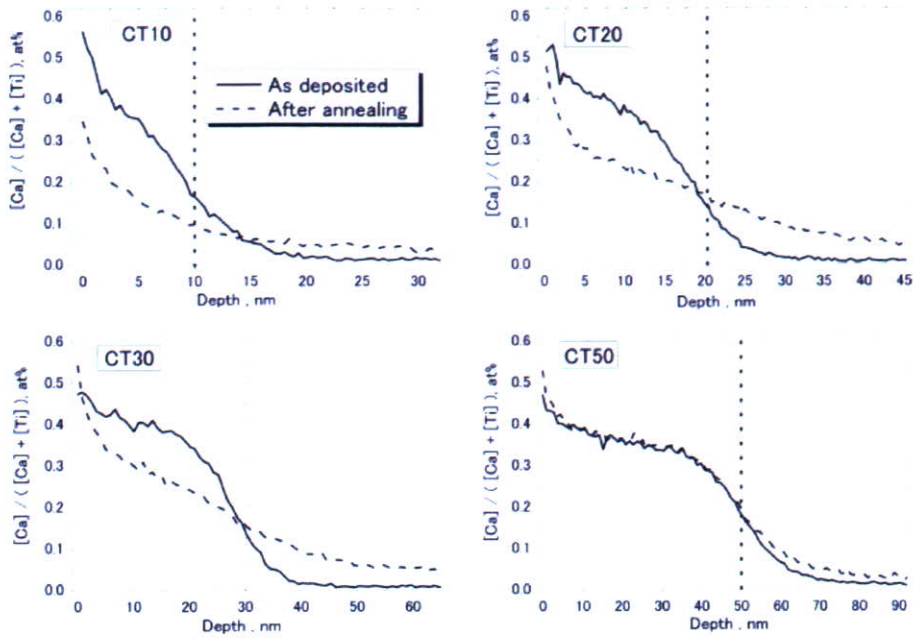

Figure 2. In-depth profiles of the Ca-atomic ratio determined by AES in CT10, CT20, CT30, and CT50 before and after annealing.

GI-XRD analysis at $\alpha = 1°$ is larger than the thickness of the $CaTiO_3$ film, the GI-XRD patterns include the peaks from both the $CaTiO_3$ film and the substrate and the interface layer explained. Perovskite-type $CaTiO_3$ peaks are only observed on CT50. Peaks originating from rutile-type TiO_2 and Ti_2O are observed in all specimens. Judging from the AES in-depth profiles in Figure 1, TiO_2 and Ti_2O as the interface layer are formed between the $CaTiO_3$ film and the Ti surface by oxidation of Ti.

Dissolution behavior of the $CaTiO_3$ film in a 0.8% NaCl solution

Figure 4 shows the in-depth profiles of the Ca-atomic ratio in CT20 and CT50 before and after immersion for 14 days. The profiles of CT10 and CT30 are similar to that of CT20. In CT20, the Ca-atomic ratio near and at the outermost surface decreases after immersion, although almost all other parts of the Ca still remain in the film. The in-depth profiles of CT50 before and after immersion are almost the same, indicating that CT50 hardly dissolves in the 0.8% NaCl solution.

Calcium-phosphate formation in HBSS

SEM observation of a specimen surface after immersion

On the surfaces of the specimens after immersion for 35 and 45 days in HBSS, four types of morphology were observed. These were categorized as follows: (1) no precipitates are observed on the surface (M1); (2) sphere-like precipitates with a size of several micrometer are scattered (M2); (3) surfaces are covered with sphere-like precipitates (M3); and (4) the precipitate layer grows into a thick layer (M4). The SEM images of typical morphologies of these four types are shown in Figure 5. Cracks contained in the M4-type morphology are due to an evaporation of water in a high-vacuum chamber. Since the EPMA-EDX spectra of the precipitates observed in M2, M3, and M4 included only the peaks from Ca and P, these precipitates were identified as calcium phosphates. The inserted values of [Ca]/[P] correspond to the atomic ratios of the calcium phosphate determined by EMPA-WDS. These values are the same as those of HAP ([Ca]/[P] = 1.67). It is apparent that the amount of calcium phosphate on the specimen surface increases in the order of M1, M2, M3, and M4. This fact suggests that the morphology change in the typical image corresponds to the growing stage of the calcium phosphate.

Thus, the effect of the $CaTiO_3$ film thickness on Ti on calcium-phosphate formation can be evaluated by categorizing the surface morphology after immersion in HBSS. The number of the specimens categorized by the type of surface morphology after immersion in HBSS is shown in Table III. For example, the number of cpTi in the M1 stage, 1/3, means that one third of the specimens show an M1-type morphology after immersion for 35 days in HBSS. On all cpTi specimens, only M1 and M2 stages were observed even after immersion for 45 days. Moreover, the HAP layers

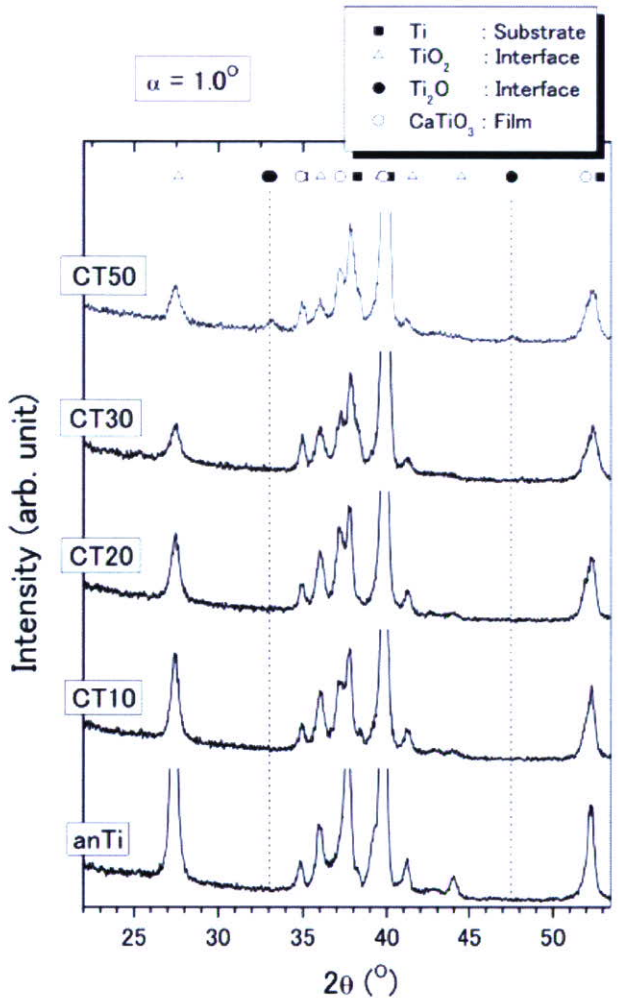

Figure 3. GI-XRD patterns of CT10, CT20, CT30, and CT50 after the annealing treatment. For comparison, the GI-XRD pattern of anTi is also included.

were not observed on these specimens by EPMA. On the CT30 specimens, only the M2 and M3 stages were observed after immersion for 35 days, although calcium phosphates grew to the M3 or the M4 stage within 45 days. On anTi, CT10, and CT20 specimens, the surface morphology changed to the M3 or M4 stage after immersion for 35 days. All CT50 specimens showed the M4 stage in 35 days. These results indicate that the performance of $CaTiO_3$-deposited titanium and annealed titanium regarding the formation of calcium phosphate is superior to that of cpTi. Moreover, the CT50 specimen seemed to show the most stable growth of the calcium phosphate layer because all of these specimens attained the M4 stage within 35 days.

SEM observation of the cross-sectional view of specimens after immersion

Figure 6 contains typical SEM images of the cross-sectional view of specimens after immersion for 45 days. Figure 6(a,b) correspond to the cross-sectional images of the M3- and M4-stage specimens, respectively. Hemisphere-like calcium phosphates are observed in Figure 6(a). No hemisphere-like shape of calcium phosphate exists in Figure 6(b); however, a uniform, thick, and dense layer is evident.

The thickness of the calcium-phosphate layer of each specimen was determined from observation of the specimens at the M4 stage after immersion for 45 days. The thickness of the calcium-phosphate layer formed on cpTi could not be determined because no specimen reached the M4 stage. The averages of the thickness of the calcium phosphate layer formed on the specimens are summarized in Figure 7. The calcium phosphate layer on the CT50 specimen is about

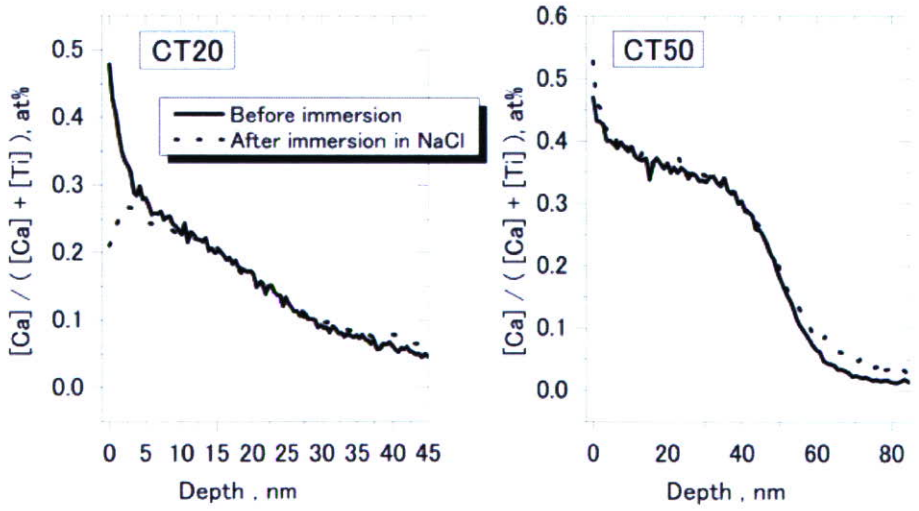

Figure 4. In-depth profiles of the Ca-atomic ratio in CT20 and CT50 before and after immersion in a 0.8% NaCl solution for 14 day.

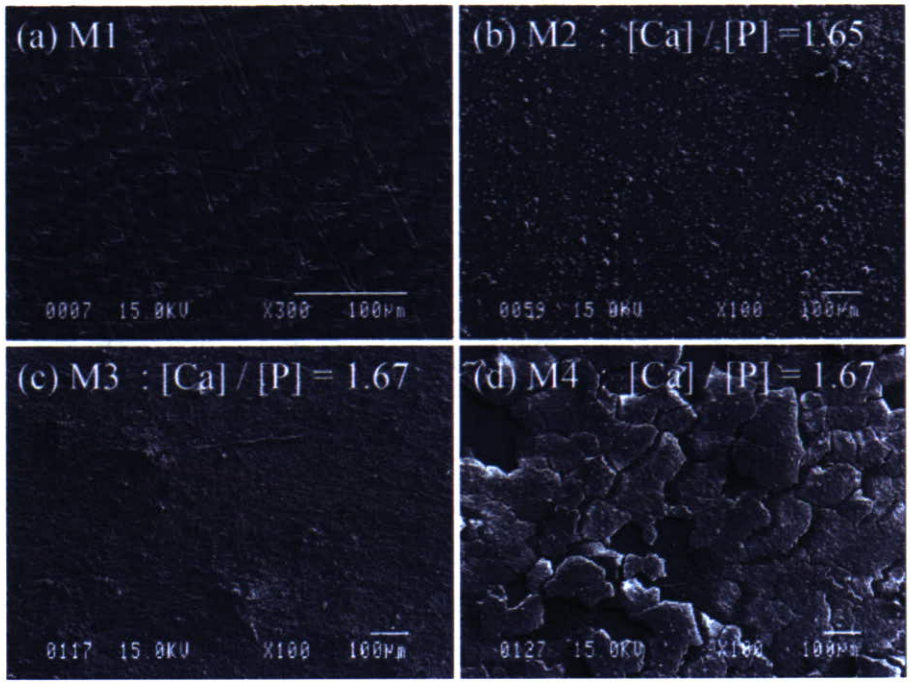

Figure 5. SEM images of the typical surface morphology of (a) M1, (b) M2, (c) M3, and (d) M4. The inserted {[Ca]/[P]} values correspond to the atomic ratios of the precipitates determined by EPMA-WDS.

twice as thick as those of the other specimens. On the other hand, the calcium-phosphate layers on the anTi, CT10, CT20, and CT30 specimens were almost identical. Consequently, the growth speed of the calcium-phosphate layer is fastest on the CT50 specimen.

Tissue responses to the specimens

Soft tissue response

Figure 8 shows the tissue response to the $CaTiO_3$ film side and the cpTi side of the specimen implanted in subcutaneous tissue at 7 and 28 days after surgery. On day 7, the granulation tissue with a slight inflammatory change was recognized on the $CaTiO_3$ film side, while fibrous connective tissue with many fibroblasts was observed on the cpTi side. The thickness of the tissue around the $CaTiO_3$ film side was thicker than that on the cpTi side [Fig. 8(a,b)]. However, no severe inflammatory responses, such as necrosis and degeneration, were observed. On day 28, the thickness of the connective tissue around the specimen became smaller on both the sides, and there was no difference between the tissue reaction on the $CaTiO_3$ film side and that on the cpTi side [Fig. 8(c,d)].

Hard tissue response

Figure 9 shows the hard tissue response to a specimen in bone marrow by optical microscopy. On day 7, fibrous tissue [white asterisk in Fig. 9(a)], including cells with large cytoplasm [black arrows in Fig. 9(a)],

TABLE III
Number of the Specimens Categorized by the Surface-Morphology Type After Immersion for 35 and 45 Days in a SBF

	After Immersion for 35 Days				After Immersion for 45 Days			
Specimens	M1	M2	M3	M4	M1	M2	M3	M4
cpTi	1/3	2/3	0/3	0/3	0/3	3/3	0/3	0/3
anTi	0/3	0/3	1/3	2/3	0/3	0/3	0/3	3/3
CT10	0/3	0/3	1/3	2/3	0/3	0/3	1/3	2/3
CT20	0/3	0/3	1/3	2/3	0/3	0/3	0/3	3/3
CT30	0/3	1/3	2/3	0/3	0/3	0/3	2/3	1/3
CT50	0/3	0/3	0/3	3/3	0/3	0/3	0/3	3/3

The fraction means number of the each growing stage divided by number of specimen.

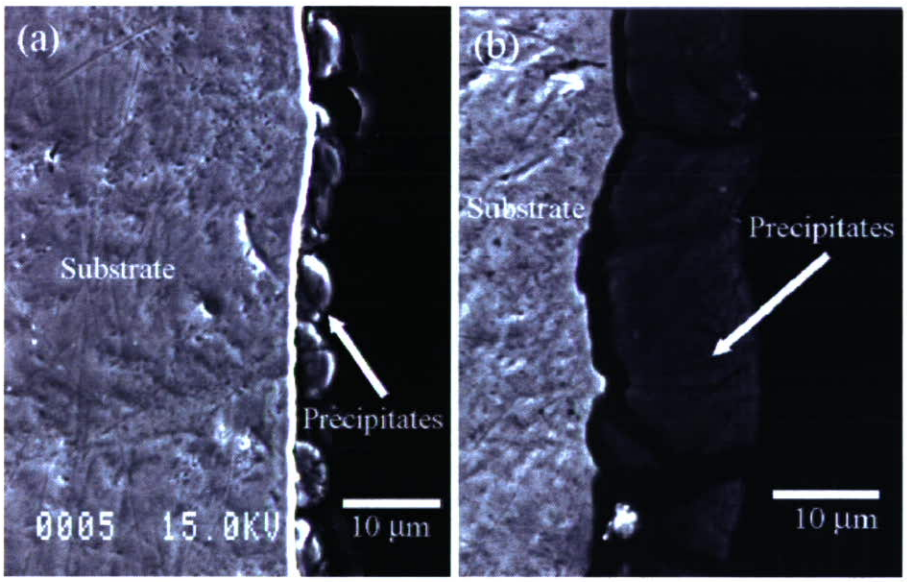

Figure 6. Typical SEM-images of cross sections of the specimens with (a) M2-stage and (b) M4-stage.

was observed on the surface of the cpTi side, and new bone [black asterisks in Fig. 9(a)] was formed away from the surface. Osteoblasts [arrowheads in Fig. 9(a)] were recognized on the surface of new bone tissue [Fig. 9(a)]. On the other hand, newly formed bone [black asterisks in Fig. 9(b)] was directly in contact with the surface of on the $CaTiO_3$ side, and many osteoblasts with a square cell shape [arrow heads in Fig. 9(b)] were observed on the osteoid [white arrows in Fig. 9(b)] formed on it [Fig. 9(b)]. On day 28, newly formed bone [black asterisk in Fig. 9(c)] on the cpTi side was remodeled to thinner, while it contacted with the surface directly [Fig. 9(c)]. In addition, on the $CaTiO_3$ side, bone remodeling on the surface progressed, and new bone [black asterisk in Fig. 9(d)] became thinner, as on the cpTi side [Fig. 9(d)].

Figure 10 shows osteogenesis around the specimen in bone marrow on day 7 by fluorescent microscopy. On the cpTi side, a slight amount of TC was deposited on the new bone away from the surface of the specimen [Fig. 10(a)]. On the other hand, in the $CaTiO_3$ film side, diffused TC deposition was observed on the new bone formed directly on the surface [Fig. 10(b)]. CA deposition was recognized on the surface of the bone away from the specimens [Fig. 10(b)].

DISCUSSION

The results from GI-XRD and AES showed that only the CT50 specimen was crystallized to perovskite-type $CaTiO_3$ after the annealing treatment. By annealing in air, the $CaTiO_3$ films were reconstructed, and the crystallinity increased. Simultaneously, Ca in the $CaTiO_3$ film diffused in the direction of the Ti substrate. In CT10, CT20, and CT30 specimens, because of the excessively thin thickness, deficiency of Ca in the $CaTiO_3$ film occurred by Ca diffusion, and the $CaTiO_3$ films were unable to form crystalline $CaTiO_3$. A $CaTiO_3$ film prepared by the RF magnetron sputtering method without any heat treatment reportedly failed to crystallize, and heating over 873 K was required to obtain a crystallized $CaTiO_3$ film.[30,34] Therefore, to obtain a crystallized perovskite-type $CaTiO_3$ thin film, $CaTiO_3$ must be deposited to at least 50 nm in thickness followed by annealing at or above 873 K.

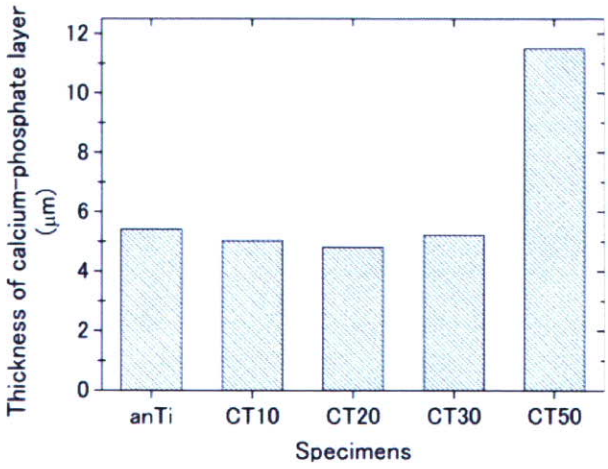

Figure 7. Average of the thickness of the calcium-phosphate layer observed on specimens showing the M4-type surface morphology after 45-days immersion.

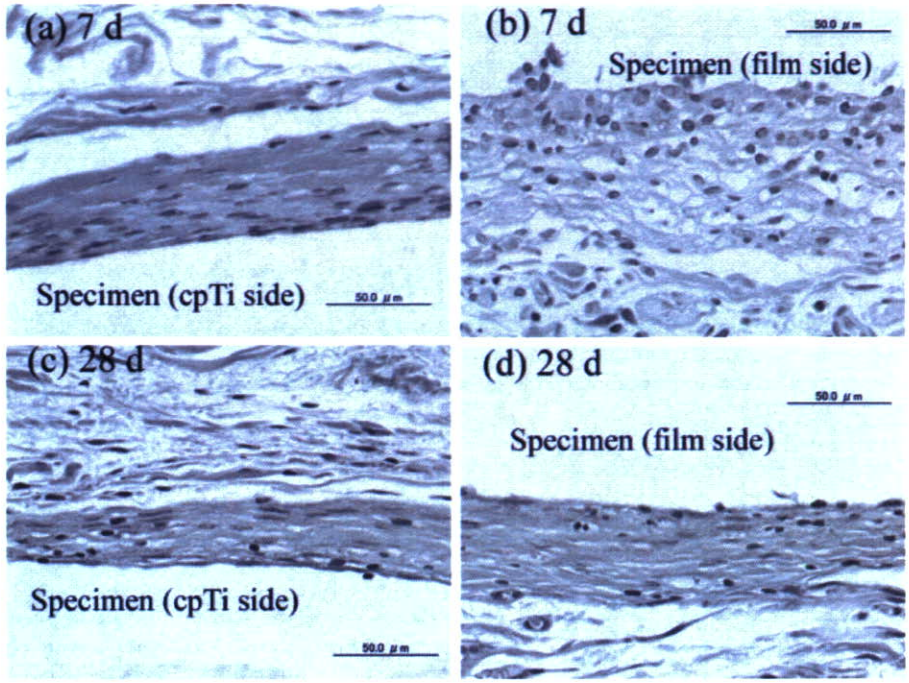

Figure 8. Soft tissue response to specimen in subcutaneous tissue after 7 and 28 days observed by optical microscopy: (a) cpTi side, day 7; (b) $CaTiO_3$ film side, day 28; (c) cpTi side, day 7; (d) $CaTiO_3$ film side, day 28.

The categorization by surface morphologies appears to be related with the nucleation of calcium phosphate. To express the performance of the nucleation of calcium phosphates numerically, a value of the growth degree was assigned to each growing stage observed in Figure 5. Values of 0, 1, 2, and 3 are

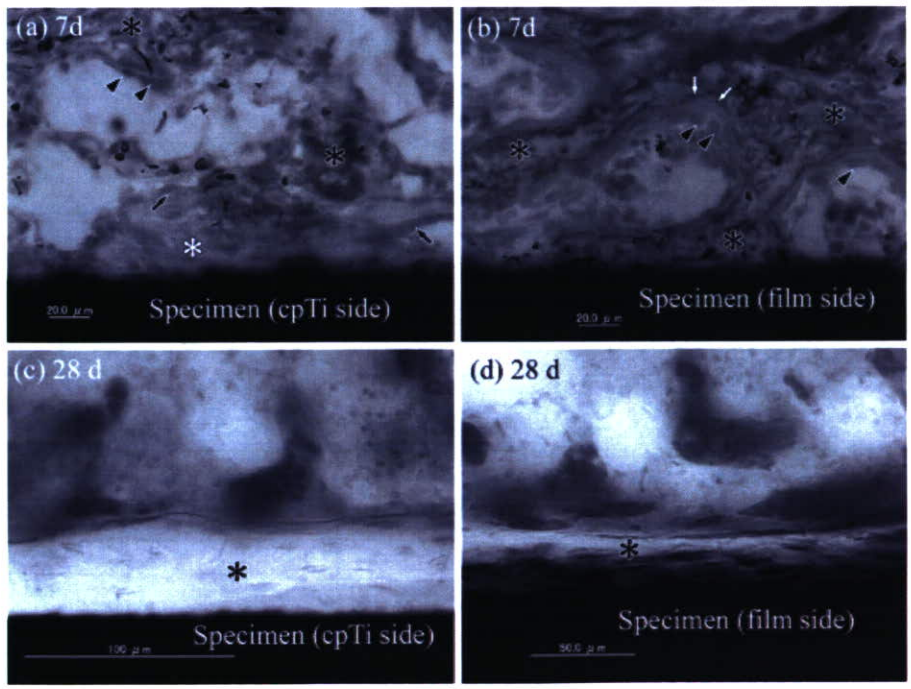

Figure 9. Hard tissue response to the specimen in femoral bone marrow after 7 and 28 days observed by optical microscopy: (a) cpTi side, 7 days; (b) $CaTiO_3$ film side, 7 day; (c) cpTi side, 28 day; (d) $CaTiO_3$ film side, 28 day.

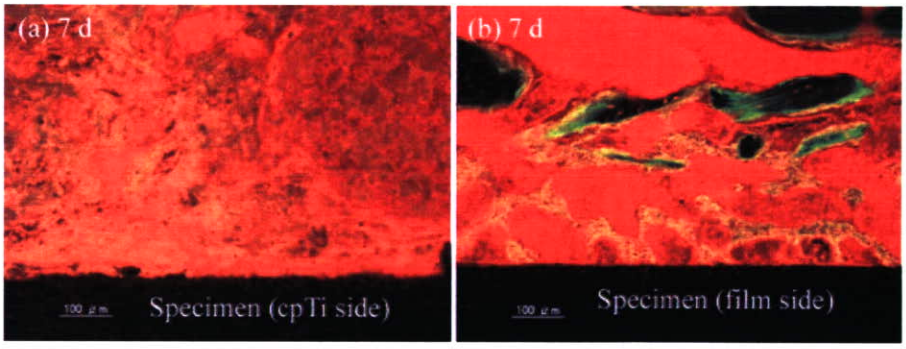

Figure 10. Hard tissue response to the specimen in femoral bone marrow after 7 days observed by fluorescent microscopy: (a) cpTi side; (b) $CaTiO_3$ film side.

assigned to the M1-, M2-, M3-, and M4-stages, respectively. The performance of each specimen was simply expressed by the sum of these values after 35- and 45-days immersion. Thus, the equation is expressed as follows:

$$\text{Performance of the nucleation of calcium phosphates} = \sum_i n_i p_i,$$

where n_i is the number of the i-type morphology and p_i is the value assigned to the i-type morphology. The thickness of the calcium-phosphate layer after immersion appears to be related with the growth rate of calcium phosphate from the nucleus. The thickness of the calcium-phosphate layer after 45-days immersion of each specimen is plotted against the performance of the nucleation of calcium phosphates in Figure 11. A good correlation between the thickness of the calcium-phosphate layer and the performance of the nucleation of calcium phosphates is observed. Judging from Figure 11, the CT50 specimen is clearly superior to the other specimens. Accordingly, it is concluded that a 50-nm $CaTiO_3$ film can enhance the performance most effectively and that 50 nm is the optimum thickness from among all the prepared thicknesses in this study. On the other hand, the performance of $CaTiO_3$ films with thicknesses of 10, 20, and 30 nm was similar to that of the annealed cpTi.

Only the CT50 specimen was crystallized to perovskite-type $CaTiO_3$. It can therefore be concluded that the good performance of the CT50 specimen regarding calcium-phosphate formation is due to this property. On the other hand, since the GI-XRD patterns of CT10, CT20, and CT30 specimens, which contained only Ti and Ti-oxide peaks, were similar to that of the anTi specimen, the calcium included in these specimens was unable to achieve the crystallized phase even after annealing. These results from the surface characterization of CT10, CT20, and CT30 specimens were similar to those of calcium-ion-implanted titanium, which had good performance regarding calcium-phosphate formation.[35] The good calcium-phosphate formation of calcium-ion-implanted titanium was reportedly due to calcium dissolution from the surface.[36] The presence of calcium dissolution from the CT20 specimen shown in Figure 4 is restricted to only the surface area, and the amount of the calcium dissolution would be less than that of calcium-ion-implanted titanium. Thus, it is suspected that calcium in CT10, CT20, and CT30 specimens has no effects on the performance regarding calcium-phosphate formation. Consequently, the performance of CT10, CT20, and CT30 specimens regarding calcium-phosphate formation is similar to that of the anTi specimen.

No severe inflammatory response, such as necrosis and degeneration, was observed on the cpTi side and the $CaTiO_3$ film side, while the tissue reaction around on the cpTi was slighter than that on the $CaTiO_3$ side

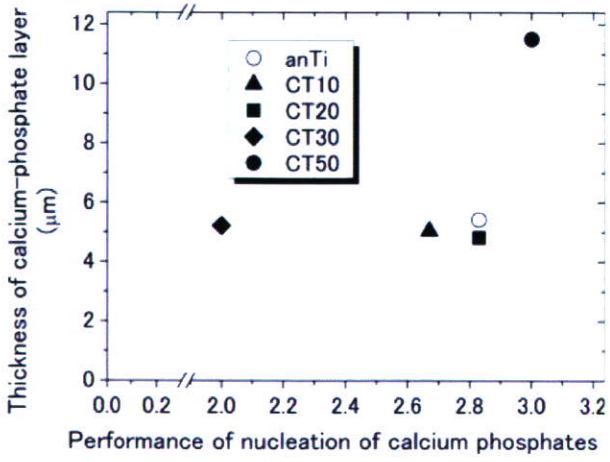

Figure 11. Correlation between the thickness of calcium-phosphate layer after 45-day immersion and the performance of the nucleation of calcium phosphates.

in subcutaneous tissue. However, after 28 days, there was no difference regarding tissue reaction between both sides. The slight inflammatory reaction on the $CaTiO_3$ film side seemed to be caused by the microstructure of the surface. The surface roughness was reported to relate to the tissue reaction.[37] However, these reactions might be bioactive and favorable to osteogenesis on the surface. In bone marrow, active bone formation was recognized on the surface of the $CaTiO_3$ film on day 7, and thinner bone was observed on the $CaTiO_3$ film on day 28. These results suggested that the $CaTiO_3$ film affected osteogenesis within the early stages and that newly formed bone was remodeled on that basis. Active bone formation on the $CaTiO_3$ film at the early implant stage might be related to the calcium phosphate precipitation occurring in HBSS. Osteogenesis on the $CaTiO_3$ film was similar to the bone formation process on HAP-coated and calcium-ion-implanted titanium.[38] These results suggest that $CaTiO_3$-coated titanium has sufficient biocompatibility and potential as a biomaterial.

Therefore, it is concluded that a $CaTiO_3$ coating on titanium could facilitate new bone formation and shorten the bone-fixation term of titanium.

CONCLUSION

A $CaTiO_3$ thin film of 50-nm in thickness deposited on titanium using RF magnetron sputtering followed by annealing at 873 K in air facilitated most effectively the calcium-phosphate formation on titanium in a simulated body fluid. On the other hand, the performance of the $CaTiO_3$ film with a thickness of less than 50 nm was inferior to that of the 50-nm-thick film. Only a 50-nm-thick $CaTiO_3$ film can be crystallized to perovskite-type $CaTiO_3$. The crystallized $CaTiO_3$ coating is required to facilitate effective calcium-phosphate formation on titanium. A $CaTiO_3$ thin film with a thickness of less than 50 nm cannot be crystallized to $CaTiO_3$ by an annealing treatment. The surface properties and performance of these films in HBSS regarding calcium-phosphate formation are similar to those of titanium annealed at 873 K.

No severe inflammatory response to titanium coated with a 50-nm-thick $CaTiO_3$ film was observed in either soft or hard rat tissue. The $CaTiO_3$ coating has sufficient biocompatibility for use as a biomaterial. In hard rat tissue, new bone formation on $CaTiO_3$-coated titanium was more active than that on noncoated titanium, and the bone directly bound to the specimen. The 50-nm-thick $CaTiO_3$ coating is an excellent surface modification method for the facilitation of new bone formation on titanium and can be expected to offer an alternative method to plasma-sprayed HAP.

The authors gratefully acknowledge Mr. Yoshihiro Murakami for operating the EPMA and the Instrument Development Core of the Institute for Materials Research, Tohoku University, for supporting the preparation of specimens.

References

1. Yamamoto A, Honma R, Sumita M. Cytotoxicity evaluation of 43 metal salts using murine fibroblasts and osteoblastic cells. J Biomed Mater Res 1998;39:331–340.
2. Kuroda D, Niinomi M, Morinaga M, Kato Y, Yashiro T. Design, mechanical properties of new β type titanium alloys for implant materials. Mater Sci Eng A 1998;243:244–249.
3. Okazaki Y, Rao S, Tateishi T, Ito Y. Cytocompatibility of various metal and development of new titanium alloys for medical implants. Mater Sci Eng A 1998;243:250–256.
4. Okazaki Y, Rao S, Ito Y, Tateishi T. Corrosion resistance, mechanical properties, corrosion fatigue strength and cytocompatibility of new Ti alloys without Al and V. Biomaterials 1998;13:1197–1215.
5. Speck KM, Fracker AC. Anodic polarization behavior of Ti–Ni and Ti-6Al-4V in simulated physiological solutions. J Dent Res 1980;59:1590–1595.
6. Nakayama Y, Yamamuro T, Kotoura Y, Oka M. In vivo measurement of anodic polarization of orthopedic implant alloys—Comparative-study of in vivo and in vitro experiments. Biomaterials 1989;10:420–424.
7. Okazaki Y, Gotoh E. Comparison of metal release from various metallic biomaterials in vitro. Biomaterials 2005;26: 11–21.
8. De Lange G, De Putter C. Structure of the bone interface to dental implants in vivo. J Oral Implantol 1993;19:123–135.
9. Jasen JA, van der Waerden JP, de Groot K. Development of a new percutaneous access device for implantation in soft tissue. J Biomed Mater Res 1991;25:1535–1545.
10. Denissen HW, de Groot K, Makkes PC, van den Hooff A, Klopper PJ. Tissue response to sense apatite implants in rats. J Biomed Mater Res 1980;14:713–721.
11. Jarcho M. Calcium phosphate ceramics as hard tissue prosthetics. Clin Orthop Relat Res 1981;157:259–278.
12. Tsui YC, Doyle C, Clyne TW. Plasma sprayed hydroxyapatite coatings on titanium substrates, Part 1: Mechanical properties and residual stress levels. Biomaterials 1998;19: 2015–2029.
13. Locardi B, Pazzaglia UE, Gabbi C, Profilo B. Thermal behavior of hydroxyapatite intended for medical applications. Biomaterials 1993;14:437–441.
14. Yamashita K, Yonehara E, Ding X, Nagai M, Umegaki T, Matsuda M. Electrophoretic coating of multilayered apatite composite on alumina ceramics. J Biomed Mater Res 1998;43: 46–53.
15. Yoshinari N, Ohtsuka Y, Derand T. Thin hydroxyapatite coating produced by the ion beam dynamic mixing method. Biomaterials 1994;15:529–535.
16. Ong JL, Lucas LC. Post-deposition heat treatments for ion beam sputter deposited calcium phosphate coatings. Biomaterials 1994;15:337–341.
17. van Dijk K, Schaeken HG, Wolke JGG, Jansen JA. Influence of annealing temperature on RF magnetron sputtered calcium phosphate coatings. Biomaterials 1996;17:405–410.
18. De Groot K, Geesink R, Klein CP, Serekian P. Plasma sprayed coatings of hydroxylapatite. J Biomed Mater Res 1987;21: 1375–1381.
19. Lin JHC, Liu ML, Ju CP. Structure and properties of hydroxyapatite–bioactive glass composites plasma sprayed on Ti-6Al-4V. J Mater Sci Mater Med 1994;5:279–283.

20. Brossa F, Cigada A, Chiesa R, Paracchini L, Consonni C. Adhesion properties of plasma sprayed hydroxyapatite coatings for orthopaedic prostheses. Biomed Mater Eng 1993;3:127–136.
21. Inadome T, Hayashi K, Nakashima Y, Tsumura H, Sugioka Y. Comparison of bone-implant interface shear strength of hydroxyapatite-coated and alumina-coated metal implants. J Biomed Mater Res 1995;29:19–24.
22. Hayashi K, Inadome T, Tsumura H, Nakashima Y, Sugioka Y. Effect of surface roughness of hydroxyapatite-coated titanium on the bone-implant interface shear strength. Biomaterials 1994;15:1187–1191.
23. Geesink RGT, de Groot K, Klein CP. Bonding of bone to apatite-coated implants. J Bone Joint Surg Br 1988;70:17–22.
24. Radin SR, Ducheyne P. Plasma spraying induced changes of calcium phosphate ceramic characteristics and the effect on in vitro stability. J Mater Sci Mater Med 1992;3: 33–42.
25. Ducheyne P, Radin S, King L. The effect of calcium phosphate ceramic composition and structure on in vitro behavior. I. Dissolution. J Biomed Mater Res 1993;27:25–34.
26. Ong JL, Lucas LC. Post-deposition heat treatment for ion beam sputter deposited calcium phosphate coatings. Biomaterials 1992;15:337–341.
27. Yoshinari M, Ohtsuka Y, Derand T. Thin hydroxyapatite coating produced by the ion beam dynamic mixing method. Biomaterials 1994;15:529–535.
28. de Groot K, Geesink R, Klein CPA, Serekian P. Plasma sprayed coating of hydroxylapatite. J Biomed Mater Res 1987;21: 1375–1381.
29. Geesink RGT, de Groot K, Klein CPAT. Chemical implant fixation using hydroxyl-apatite coatings. The development of a human total hip prosthesis for chemical fixation to bone using hydroxyl-apatite coatings on titanium substrates. Clin Orthop Relat Res 1987;225:147–170.
30. Ohtsu N, Sato K, Saito K, Asami K, Hanawa T. Calcium phosphates formation on $CaTiO_3$ coated titanium. J Mater Sci Mater Med. Forthcoming.
31. Ohtsu N, Sato K, Saito K, Hanawa T, Asami K. Evaluation of degradability of $CaTiO_3$ thin film in simulated body fluids. Mater Trans 2004;45:1778–1781.
32. Ohtsu N, Ashino T, Asami K. Silicon contamination adsorbed o pure titanium plate during soaking test in Hanks' balanced saline solution. Mater Trans 2004;45:550–553.
33. Yokoyama A, Matsumoto H, Yamamoto S, Kawasaki T, Kohgo T, Uo M, Watari F, Nakasu M. Tissue response to a newly developed calcium phosphate cement containing succinic acid and carboxymethyl-chitin. J Biomed Mater Res A 2003;64:491–501.
34. Ohtsu N, Saito K, Asami K, Hanawa T. Characterization of $CaTiO_3$ thin film prepared by ion-beam assisted deposition. Surf Coat Technol 2006;200:5455–5461.
35. Hanawa T, Murakami K, Kihara S. Calcium Phosphate Precipitation on Calcium-Ion-Implanted Titanium in Electrolyte. In: Horowitz E, Parr JE, editors. Characterization and Performance of Calcium Phosphate Coatings for Implant. Philadelphia: American Society for Testing and Materials; 1994. p 170. ASTM STP 1196.
36. Hanawa T, Asami K, Asaoka K. Microdissolution of calcium ions from calcium-ion-implanted titanium. Corros Sci 1996;38: 1579–1594.
37. Parker J, Walboomers X, Von den Hoff J, Maltha J. Soft-tissue response to silicone and poly-L-lactic acid implants with a periodic or random surface micropattern. J Biomed Mater Res 2002;61:91–98.
38. Hanawa T, Kamiura Y, Yamamoto S, Kohgo T, Amemiya A, Ukai H, Murakami K, Asaoka K. Early bone formation around calcium ion implanted titanium inserted into rat tibia. J Biomed Mater Res 1997;36:131–136.